

<https://doi.org/10.1038/s44172-024-00200-9>

A ghost imaging framework based on laser mode speckle pattern for underwater environments

Check for updates

Mo-Chou Yang, Peng Wang, Yi Wu & Guo-Ying Feng

Due to the complex physical processes found in underwater environments, such as absorption, scattering, and noise, it is challenging to obtain high-quality images using conventional camera-based imaging techniques. Ghost imaging possesses strong anti-interference capabilities and can effectively obtain images in underwater environments. Here, we propose a ghost imaging framework based on a physical model of M^2 -ordered laser mode patterns and apply it to Ghost Imaging. The simulation results show that the Laser Mode Speckle Ghost Imaging can reconstruct the overall trapped contour even at a low sampling rate, specifically below 0.64%. A high-quality image with a Peak Signal-to-Noise Ratio of 19 dB can be achieved using the Laser Mode Speckle Ghost Imaging when the sampling rate is 5%. Even with a relative random noise of 1.0%–5.0%, the imaging quality of Laser Mode Speckle Ghost Imaging is superior to that of Random speckle pattern Ghost Imaging, Walsh speckle pattern Ghost Imaging, and Haar speckle pattern Ghost Imaging when the sampling rate consistent. Our experimental results in a turbid water environment confirm the conclusions drawn from the simulation results. The proposed Laser Mode Speckle Ghost Imaging can be used as an imaging solution in challenging liquid environments, such as turbid liquids, inclement weather, and biological tissue fluids.

When performing target detection in underwater environments, the complexity of the underwater environment, including physical factors such as absorption, scattering, and noise, as well as the low sensitivity of the detector, results in low imaging quality when using conventional camera-based imaging techniques. As a result, there are greater difficulties in discovering and recognizing objects in these environments. Ghost imaging (GI) technology is a modern method that can produce high-quality images in complex environments, and it relies on the illumination speckle pattern for its realization. In GI, objects are illuminated with speckle patterns, which are subsequently collected by a bucket detector without spatial resolution. These patterns are used to form a reconstructed image through correlation calculation. Owing to its wide range of light sources and strong anti-interference ability, GI has attracted significant attention in several related fields such as X-ray imaging^{1,2}, terahertz imaging³, acoustic imaging⁴, three-dimensional imaging^{5,6}, fluorescence imaging¹, optical encryption^{7,8}, and underwater imaging^{9–15}. The application scenarios and influencing factors of GI are depicted in Fig. 1.

Recently, researchers have discussed the effect of speckle patterns on GI^{16,17}. According to mathematical distribution, modulated speckle patterns can be classified into random and orthogonal types. Scholars have utilized various random speckle patterns in GI, including Gaussian random type¹⁸, Bernoulli random type¹⁹, pink noise type²⁰, and orthogonal speckle patterns such as the Fourier type²¹, Hadamard type²², Walsh type²³, rearranged Hadamard type²⁴, Hadamard–Haar type²⁵, “average sparsity”²⁶, and cosinusoidal-encoding multiplexed type^{27,28}. Typically, random speckle patterns should satisfy the Nyquist theorem when performing correlation calculations. In other words, effective imaging can only be achieved when the sampling rate is two. However, orthogonal speckle patterns can achieve perfect imaging when the sampling rate is one. These speckle patterns typically necessitate a higher sampling rate to achieve better imaging quality, which results in a significant time consumption when excluding non-interested targets. The efficiency of detecting interested targets in complex underwater environments still needs improvement.

Here, we propose a ghost imaging framework based on the physical model of M^2 -ordered laser mode patterns and adopt the GI

Institute of Laser & Micro/Nano Engineering, College of Electronics and Information Engineering, Sichuan University, Chengdu, Sichuan 610065, China.

 e-mail: guoqing_feng@scu.edu.cn

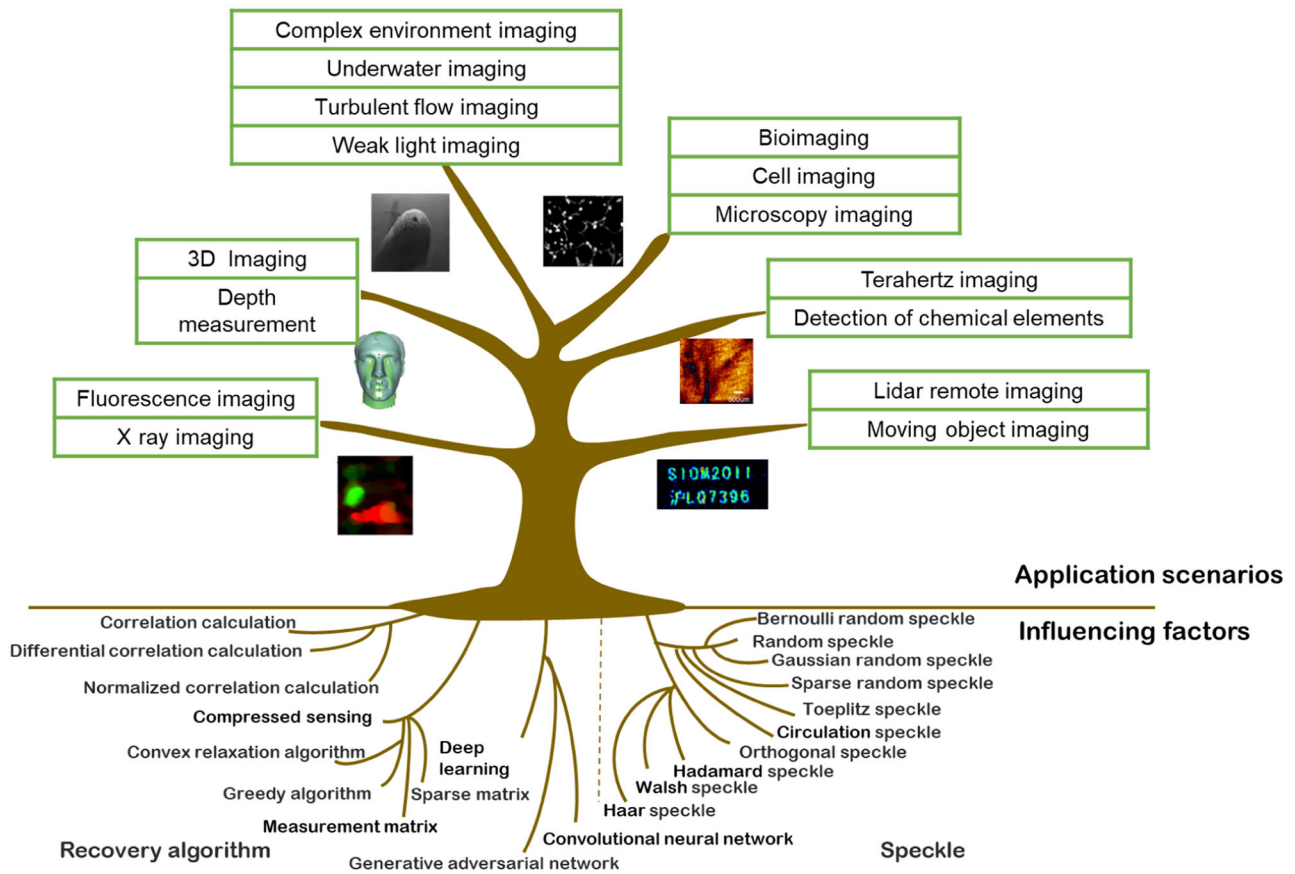


Fig. 1 | Schematic diagram of influencing factors and application scenarios of ghost imaging (GI). The influencing factors mainly include the speckle patterns and recovery algorithm, and the application scenarios mainly include 3D imaging⁵, fluorescence imaging¹, lidar²⁹, terahertz imaging³, bioimaging³⁰, and underwater imaging¹⁰.

method for underwater monitoring complex environments. Laser mode speckle pattern GI (LMS-GI) can quickly capture most of the information from unknown targets at a low sampling rate, filter out irrelevant targets, and then perform imaging on the targets of interest. This method can significantly improve the speed of detecting the targets of interest in complex underwater environments. Furthermore, LMS-GI is highly robust and outperforms conventional GI in real underwater environments. In highly turbid underwater environments, it can achieve low-sampling imaging comparable to that obtained using compressed sensing and deep learning. In the future, LMS-GI could be extensively utilized in remote sensing, bioimaging, and other fields because of its low sampling rate and high imaging quality.

Results
Laser modes

In a Cartesian coordinate system (x, y, z) , the paraxial Helmholtz equation is:

$$\frac{\partial^2 E}{\partial x^2} + \frac{\partial^2 E}{\partial y^2} + 2ik \frac{\partial E}{\partial z} = 0 \tag{1}$$

where $E(x, y, z)$ is the slow-varying amplitude of the electric field, $k^2 = k_0^2 n^2$, $k_0 = 2\pi/\lambda$ is the number of the waves in a vacuum, λ is the wavelength, and n is the refractive index of the medium. The solutions to the paraxial wave equation in Cartesian coordinates are the Hermitian-Gaussian (H – G) laser modes with an orthogonal unification completeness, referred to as H – G_{mn} mode. For a square spherical mirror symmetrical confocal cavity with a side length of $2a$ and a cavity length of L ,

the mathematical expression of a H – G_{mn} laser mode is as below,

$$E_{mn}(x, y) = C_{mn} H_m \left(\sqrt{\frac{2\pi}{L\lambda}} x \right) H_n \left(\sqrt{\frac{2\pi}{L\lambda}} y \right) e^{-\frac{x^2+y^2}{L\lambda}} \tag{2}$$

where m and n are indices of laser modes. $m + 1$ represents the number of nodes in the x direction, and $n + 1$ represents the number of nodes in y direction. C_{mn} is the normalized constant of the H- G_{mn} mode. H_m and H_n are the m -th and n -th order Hermite polynomials, respectively.

$$H_m(X) = \sum_{k=0}^{\lfloor \frac{m}{2} \rfloor} \frac{(-1)^k m!}{k!(m-2k)!} (2X)^{m-2k} \tag{3}$$

$$H_n(Y) = \sum_{k=0}^{\lfloor \frac{n}{2} \rfloor} \frac{(-1)^k n!}{k!(n-2k)!} (2Y)^{n-2k}$$

where $\lfloor \frac{m}{2} \rfloor$ is the integer part of $\frac{m}{2}$, $\lfloor \frac{n}{2} \rfloor$ is the integer part of $\frac{n}{2}$, $X = \frac{\sqrt{c}}{a} x, Y = \frac{\sqrt{c}}{a} y, c = 2\pi N$, and the Fresnel number $N = a^2/(\lambda L)$. The two-dimensional intensity distributions and three-dimensional complex amplitude distributions of H- G_{00} to H- G_{33} laser modes are shown in Fig. 2a.

Siegman introduced the concepts of spatial frequency and intensity moment while establishing a relatively complete theoretical model for the concept of the M^2 factor used to evaluate laser beam quality²⁹⁻³¹. The M^2 factor has become one of the most widely accepted parameters for evaluating the beam quality of laser beams³²⁻³⁵. The waist radius and the far-

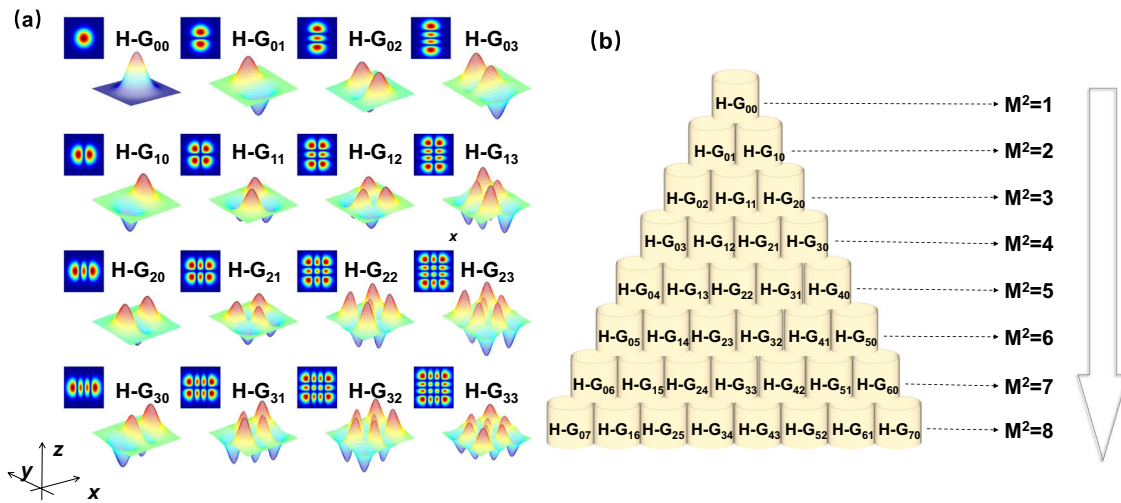


Fig. 2 | Hermitian-Gaussian (H-G) $_{00} \sim H-G_{33}$ modes and their sorting by M_{mn}^2 values. a The two-dimensional intensity distributions and three-dimensional complex amplitude distributions of $H-G_{00} \sim H-G_{33}$ modes. **b** $H-G_{mn}$ laser modes are sorted according to their M_{mn}^2 values.

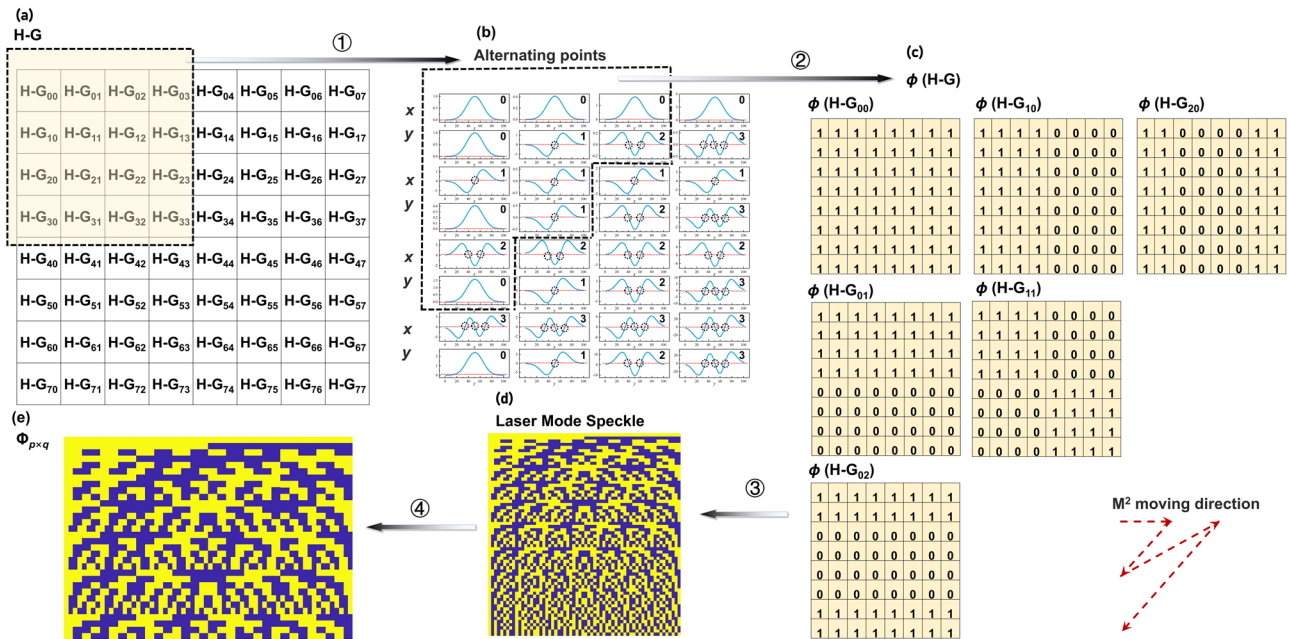


Fig. 3 | Formation process of laser mode speckle patterns. a Structure diagram of Hermitian-Gaussian ($H-G_{00} \sim H-G_{77}$ mode. **b** Zero change point of amplitude in $H-G_{00} \sim H-G_{33}$ mode. **c** Checkerboard pattern of the two-phase values 0 and 1. for $M_{mn}^2 \leq 3$. **d** Complete laser speckle patterns at an 8×8 resolution. **e** Part of laser mode speckle patterns at an 8×8 resolution.

field divergence half-angle of the fundamental Gaussian $H-G_{00}$ laser mode are set as w_0 and θ_0 , and

$$w_0 \theta_0 = \frac{\lambda}{\pi} \tag{4}$$

The waist radii of the $H-G_{mn}$ laser mode in the x direction, y direction and the r radial direction ($r^2 = x^2 + y^2$, which represents the square of the distance of a point (x, y) from the propagation axis z), are:

$$\begin{aligned} w_{0x,mn}^2 &= (2m + 1)w_0^2 \\ w_{0y,mn}^2 &= (2n + 1)w_0^2 \end{aligned} \tag{5}$$

The waist radii of the $H - G_{mn}$ laser mode in the r radial direction is:

$$w_{0r,mn}^2 = 2(m + n + 1)w_0^2 \tag{6}$$

The far-field diverging half-angles of the $H-G_{mn}$ laser mode in the x direction, y direction, and r radial direction are:

$$\begin{aligned} \theta_{x,mn} &= \sqrt{2m + 1}\theta_0 \\ \theta_{y,mn} &= \sqrt{2n + 1}\theta_0 \\ \theta_{r,mn} &= \sqrt{(2m + 1)(2n + 1)}\theta_0 \end{aligned} \tag{7}$$

The M^2 factors of H-G_{mn} laser mode in the x and y directions can be expressed as:

$$\begin{aligned} M_x^2 &= 2m + 1 \\ M_y^2 &= 2n + 1 \end{aligned} \quad (8)$$

The M^2 factors of H-G_{mn} laser beam in the r radial direction can be expressed as:

$$M_r^2 = m + n + 1 \quad (9)$$

The H-G_{mn} laser modes are sorted according to their beam quality M_{mn}^2 values from 1 to 8, as shown in Fig. 2b. The larger the value of M_{mn}^2 factor, the larger the sequential number of H-G_{mn} laser modes included. The increase in the sequential number of laser modes is characterized by a ladder shape. The fundamental laser mode H-G₀₀ ($m = n = 0$) represents a zero spatial frequency signal, while the higher order laser mode H-G_{mn} ($m \neq 0$ or $n \neq 0$) represents a higher spatial frequency signal.

Ghost imaging model

Figure 3 depicts the formation of LMS with a solution of 8×8 pixels. Figure 3a shows the matrix distribution of 64 modes (H-G₀₀ ~ H-G₇₇). 16 modes (H-G₀₀ ~ H-G₃₃) are selected for depicting numerically simulated amplitude and phase in the x and y directions, as shown in Fig. 3b. Adjacent nodes have a phase shift of π . Phase patterns from standard H-G beams were simulated, and checkerboard patterns $\varphi(H - G_{mn})$, $m = 1, \dots, q_1$, $n = 1, \dots, q_2$, two-phase values (0 and 1) based on laser modes were obtained, as shown in Fig. 3c. The speckle patterns of H-G_{mn} laser modes were sorted according to their M_{mn}^2 values, and a complete speckle pattern matrix was obtained, as shown in Fig. 3d. Part of the speckle pattern matrix is obtained after under-sampling, as shown in Fig. 3e. The $\varphi(H - G_{mn})$, $m = 1, \dots, q_1$, $n = 1, \dots, q_2$ were converted to q dimensional data. The corresponding speckle pattern

matrix is as follows:

$$\Phi = \begin{bmatrix} \varphi(H - G_{00}) \\ \varphi(H - G_{01}) \\ \vdots \\ \varphi(H - G_{q_1 q_2}) \end{bmatrix} \quad (10)$$

Imaging quality standards

We used Peak Signal-to-Noise Ratio (PSNR) and Structural Similarity (SSIM) to characterize the image quality of the GI image $G(x, y)$ which is relative to the object $T(x, y)$ being measured. The PSNR³⁶ is:

$$PSNR = 10 \log_{10} \left(\frac{q_1 q_2 \cdot MAX^2}{\sum_{x=1}^{n_1} \sum_{y=1}^{n_2} [G(x, y) - T(x, y)]^2} \right) \quad (11)$$

where MAX represents the maximum possible pixel value of the image; in this study, MAX = 255.

The SSIM³⁷ is:

$$\begin{aligned} SSIM(G, T) &= L(G, T) * C(G, T) * S(G, T) \\ L(G, T) &= \frac{2u_G u_T + C_1}{u_G^2 + u_T^2 + C_1} \\ C(G, T) &= \frac{2\sigma_G \sigma_T + C_2}{\sigma_G^2 + \sigma_T^2 + C_2} \\ S(G, T) &= \frac{\sigma_{GT} + C_3}{\sigma_G \sigma_T + C_3} \end{aligned} \quad (12)$$

where u_G and u_T are the averages of $G(x, y)$ and the object $T(x, y)$, respectively. σ_G and σ_T are the standard deviations of the GI and the object, respectively, and σ_{GT} is the covariance between the GI and the object. C_1, C_2 ,

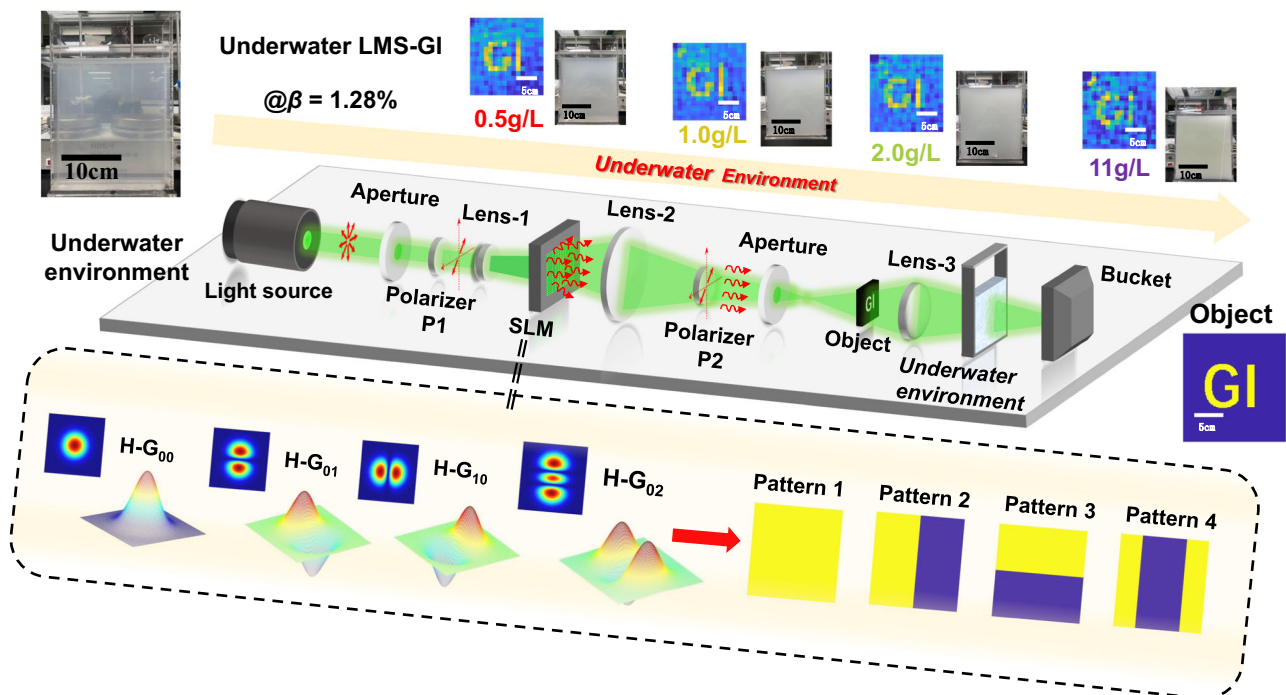


Fig. 4 | Scheme of the underwater experimental system. The proposed laser mode speckle pattern ghost imaging (LMS-GI) is a physical model based on the M^2 -sequence Hermitian-Gaussian (H-G) laser modes, and they are orthogonal.

and C_3 are constants used to guarantee that the denominator of the formula is not zero. In general, $C_1 = (K_1 L_1)^2$, $C_2 = (K_2 L_1)^2$, $C_3 = C_2/2$, $K_1 = 0.01$, $K_2 = 0.03$, and $L_1 = 255$.

Experiment setup

The underwater experimental setup of LMS-GI is shown in Fig. 4. Using a laser with a collimation system (Fuzhe Laser Technology FU532D12-BD43) as the light source, a spatial light modulator (SLM) (UPOLabs RSLM1024) was used to generate computer-controlled laser mode patterns. The power meter (OPHIR PD300-3W-V1 and OPHIR StarLite) acted as a bucket detector and was recorded by the computer. The object under test was placed at the “object” shown in Fig. 4. The focal length of lens 1 was 10 cm, the focal length of lens 2 was 15 cm, and the focal length of lens 3 was 10 cm. The dimensions of the pool were 21 cm × 31.5 cm × 4.1 cm. We added 1.0 g, 2.0 g, 4.0 g, 6.0 g, 11 g, and 22 g of milk powder to 2 L of water, and then stirred the solution using a MeiYingPu H05-1 constant temperature magnetic stirrer to form uniformly turbid water. The concentrations were as follows: 0.5 g/L, 1.0 g/L, 2.0 g/L, 3.0 g/L, 5.5 g/L, and 11 g/L, respectively. The milk powder used had a protein content of 21.2 g/100 g and a fat content of 19.3 g/100 g. At concentrations greater than 1 g/L, conventional imaging methods using CCD/CMOS became ineffective.

Figure 5 displays a partial list of the random speckle pattern matrices and orthogonal speckle pattern matrices. The inner part displayed the distribution of the speckle pattern matrix, while the outer part showed the speckle patterns for each projection.

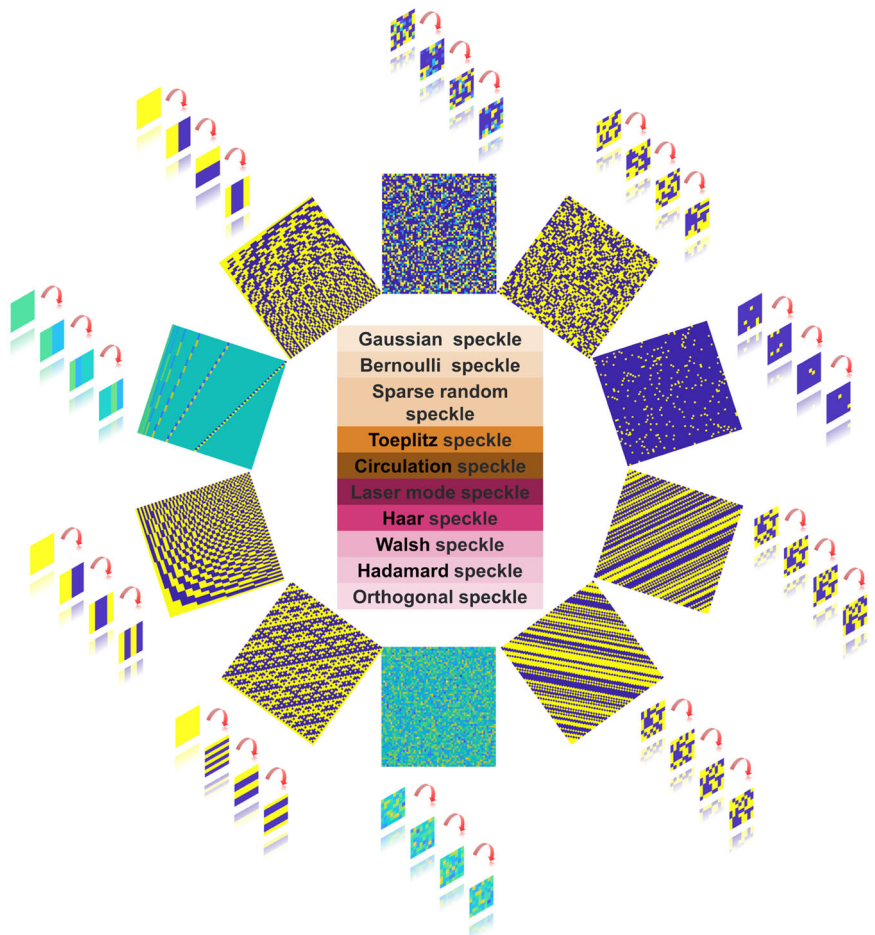
Discussion

We simulated four types of GIs for four types of objects with a distribution of 128×128 pixels. Random speckle patterns, Walsh speckle

patterns, and Haar speckle patterns were selected for comparison with our proposed LMS patterns. There are four different types of objects being tested. “ILMNE” represents the digital type, “Cell” represents the cell type, “Tumor” represents the medical type, and “Cameraman” represents the human type. The simulated results of random speckle pattern GI (Random-GI), Walsh speckle pattern GI (Walsh-GI), Haar speckle pattern GI (Haar-GI), and LMS-GI are shown in Fig. 6a. Due to the random nature of the random speckle patterns, the imaging quality for this type of GI is significantly lower than that for the other three GIs. Moreover, these three types of speckle patterns are orthogonal. Thus, perfect imaging can only be achieved at the sampling rate of $\beta = 100\%$. In addition, Walsh GI and Haar GI exhibit noticeable vertical stripe-like noise at low sampling rates. In contrast, LMS-GI can detect the overall trapped contour at a low sampling rate ($\beta = 0.64\%$). Furthermore, at a sampling rate of $\beta = 2.48\%$, the imaging results of LMS-GI fulfill the general requirements. At a slightly higher sampling rate of $\beta = 5.00\%$, details are clearly distinguishable in the “ILMNE”, “Cell”, and “Tumor”. In addition, the silhouette of the portrait in “Cameraman” is clearly visible, and the details of the camera stand are also distinct. The subjective judgment method alone is not sufficient to validate the excellent imaging quality of LMS-GI. Therefore, SSIM and PSNR analyses of the images were performed, as shown in Fig. 6b, c. In the SSIM shown in Fig. 6b, the LMS-GI value is significantly higher than that of Random-GI and Haar-GI. However, the Walsh-GI had a higher value than the LMS-GI in certain iterations of the experiment, which can be attributed to the SSIM calculation method, which can be attributed to the SSIM calculation method. In combination with the PSNR shown in Fig. 6c, the significant advantage of LMS-GI over the other GI methods at sampling rates below 10.0% is evident.

Fig. 5 | A partial list of speckle pattern matrices.

The inner ring displayed the distribution of the speckle pattern matrix, while the outer ring showed the speckle patterns for each projection.



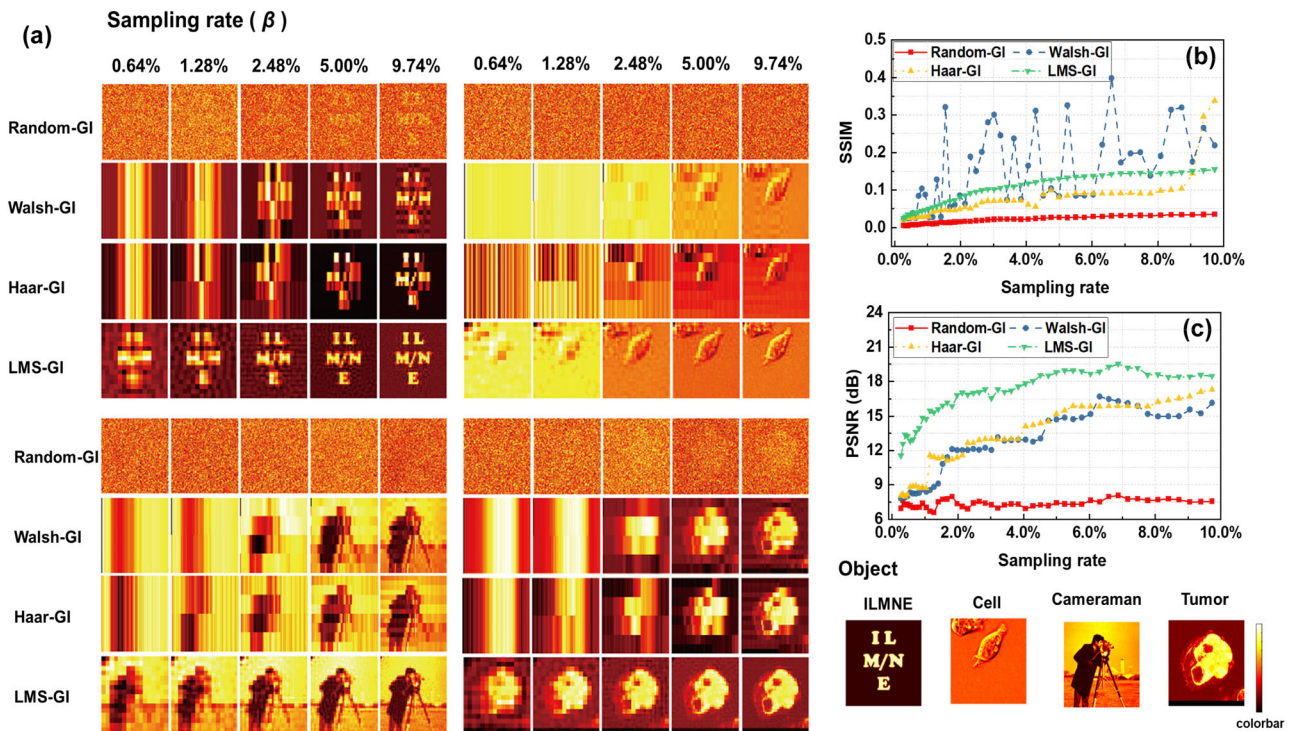


Fig. 6 | A comparison of simulated results for ghost imaging (GI). **a** Images reconstructed by Random speckle pattern GI (Random-GI), Walsh speckle pattern GI (Walsh-GI), Haar speckle pattern GI (Haar-GI), and Laser mode speckle GI (LMS-GI) at various sampling rates. There are four distinct types of objects being tested. “ILMNE” represents the digital type, “Cell” represents the cell type, “Tumor” represents the medical type, and “Cameraman” represents the human type. **b** The

calculated structural similarity indicators (SSIM) of Random-GI (red square), Walsh-GI (blue circle), Haar-GI (yellow regular triangle), and LMS-GI (green inverted triangle) versus sampling rates for object “ILMNE”, respectively. **c** The peak signal-to-noise ratio (PSNR) values were calculated for Random-GI (red square), Walsh-GI (blue circle), Haar-GI (yellow regular triangle), and LMS-GI (green inverted triangle) versus sampling rates for object “ILMNE”, respectively.

To judge the imaging robustness, we added 1.0% relative random noise to the bucket of these four types of GI, and the imaging results are shown in Fig. 7a. We added 1.0% random wave noise by averaging the received values of the bucket detector, using a multiplier operation and a random function. Combined with the data shown in Fig. 7b, it can be seen that the image quality of LMS-GI was the best at the same sampling rate, indicating its relatively superior robustness compared to the other types of GI. At this time, 1.0%, 2.0%, 3.0%, 4.0%, and 5.0% relative random noise were added to the bucket detector of LMS-GI. The imaging results at a sampling rate of 2.48% are shown in Fig. 7c. It can be seen that even with noise, the imaging quality of LMS-GI was still better than the other three ideal imaging results without noise when the sampling rate was the same. By combining the SSIM and PSNR in Fig. 7d, e, it can be observed that LMS-GI was impacted by noise, leading to a decrease in its imaging quality as the level of noise increased. However, its robustness remained reliable.

We conducted Random-GI, Walsh-GI, Haar-GI, and LMS-GI experiments in both air and milk, as shown in Fig. 8. The presence of laser and bucket detection fluctuations during the experiment resulted in uncertain random values and positions, leading to experimental results that deviated from the ideal simulated results (Fig. 6c). Overall, the imaging quality of LMS-GI was much better than that of Random-GI, Walsh-GI, and Haar-GI. In general, when using LMS-GI, the imaging quality was good when the sampling rate was 10.0% or less. When the sampling rates were 0.64%, 1.28%, and 2.48%, the results of the turbid underwater LMS-GI experiment are shown in Fig. 8b. The concentrations of turbid water were: 0.5 g/L, 1.0 g/L, 2.0 g/L, 3.0 g/L, 5.5 g/L, and 11 g/L. When a CCD/CMOS was used for imaging, there was a blur when the turbid water concentration was 0.5 g/L, and it was almost invisible when the turbid water concentration was 1.0 g/L. The imaging quality of LMS-GI was high when the turbid water concentration was less than 1.0 g/L.

When the concentration exceeded 1.0 g/L, the imaging quality decreased, but it was still possible to reconstruct the image. It can be seen that LMS-GI was still able to produce images at a low sampling rate of 0.64% in turbid water. Furthermore, the sampling rate was significantly lower than that of GI using compressed-sensing technology, and even lower than that of most deep-learning GI methods.

Table 1 provides a comparison of LMS-GI with underwater imaging GI techniques used by other researchers. The turbid water used by researchers is usually made by adding china clay or milk to water. When using china clay as the additive, the unit of turbidity measurement is Nephelometric Turbidity Unit (NTU) (1 NTU = 1 mg/L SiO₂). When milk is added, the unit of turbidity used is Formazin Turbidity Unit (FTU), with Formazin used as the standard liquid. In this study, the instructions for the milk powders indicated that conventional milk is prepared by reconstituting 35 grams of milk powder in 200 mL of water. The ratio of milk powder to water used in the above study was converted to the milk-to-water ratio used by other researchers. The results ranged from 1:1000 to 1:7, covering both low-turbidity and high-turbidity areas. According to the experimental results, it can be seen that LMS-GI can be used not only in a low-turbidity underwater environment but also in a high-turbidity underwater environment. Compared to the sampling rates used by other researchers, our sampling rate of 2.48% is not the minimum value. However, the LMS-GI’s correlation algorithm is more convenient and has a lower computation time compared to GI methods using compressed-sensing technology.

Conclusions

In this study, we have proposed orthogonal speckle patterns based on a physical model of M^2 -ordered H-G laser mode patterns and applied them to GI. Simulated and experimental results have demonstrated that the LMS-GI can achieve ultra-low sampling imaging. When the sampling rate was 5%, we achieved high-quality imaging

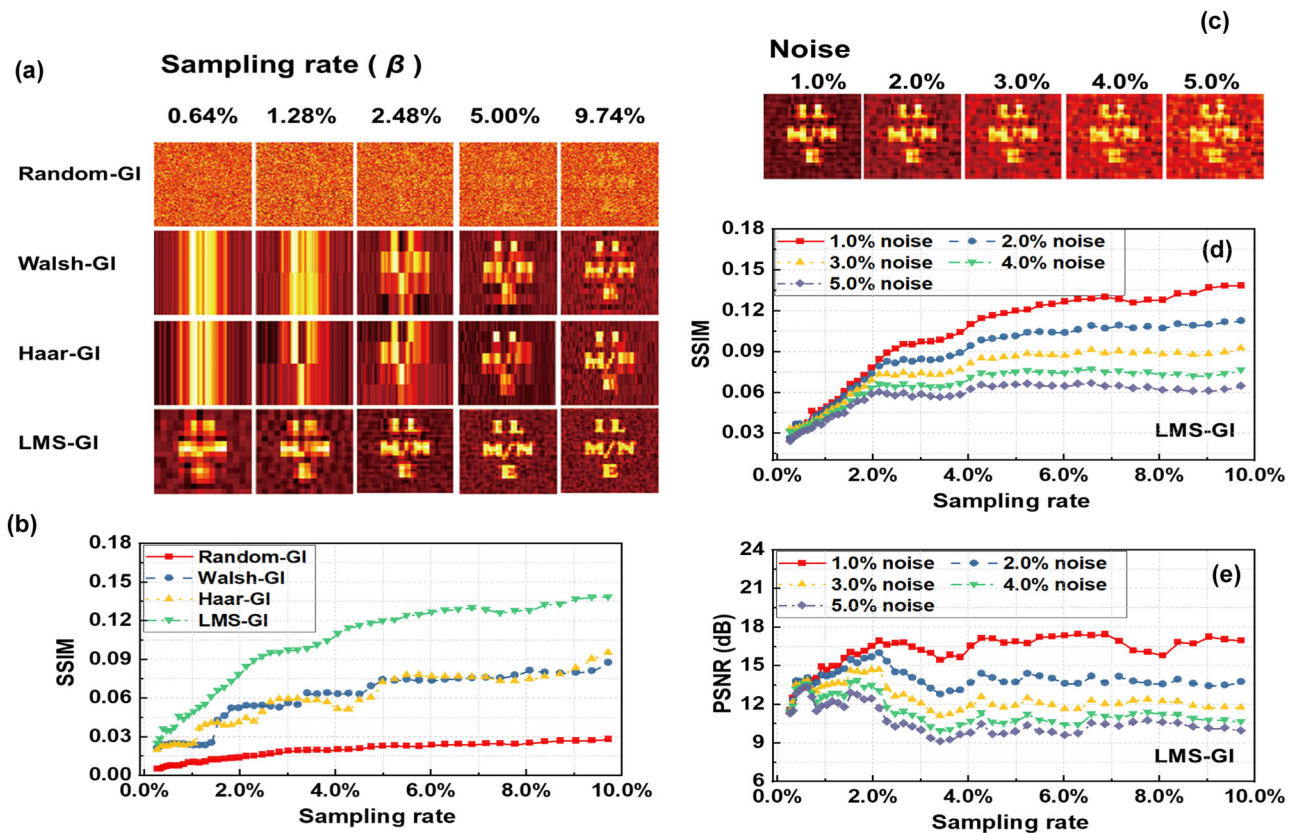


Fig. 7 | Simulated results of ghost imaging (GI) at various levels of relative random noise. **a** Images were reconstructed using Random speckle pattern GI (Random-GI), Walsh speckle pattern GI (Walsh-GI), Haar speckle pattern GI (Haar-GI), and Laser mode speckle pattern ghost imaging (LMS-GI) at various sampling rates, when a relative random noise of 1.0%. **b** The Structural Similarity (SSIM) indicators were calculated for Random-GI (red square), Walsh-GI (blue circle), Haar-GI (yellow regular triangle), and LMS-GI (green inverted triangle)

versus sampling rates at 1.0% relative random noise. **c** The images were reconstructed by LMS-GI at a sampling rate of 2.48% with 1.0% to 5% relative random noise. Calculated the SSIM (**d**) and the peak signal-to-noise ratio (PSNR) (**e**) of LMS-GI versus sampling rates at 1.0% (red square), 2% (blue circle), 3% (yellow regular triangle), 4% (green inverted triangle), and 5% (gray diamond) relative random noise levels. The object is “ILMNE”.

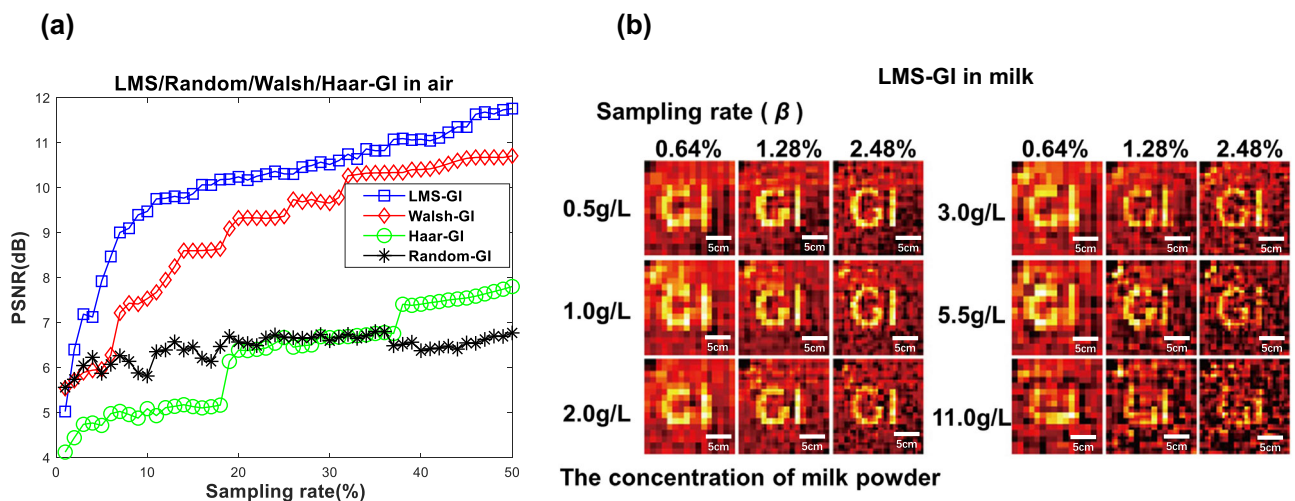


Fig. 8 | Experimental results of ghost imaging (GI). **a** Peak signal-to-noise ratio (PSNR) indicators versus sampling rates for laser mode speckle GI (LMS-GI, blue square), Walsh speckle pattern GI (Walsh-GI, red diamond), Haar speckle Pattern

GI (Haar-GI, green circle), and Random speckle pattern GI (Random-GI, black star) in air. **b** Images reconstructed by LMS-GI at various sampling rates in turbid water.

with the PSNR reaching 19 dB. However, at a sampling rate of 0.64%, a rough contour was able to be formed. The LMS-GI demonstrates strong robustness and can be used for imaging in turbid underwater environments. Compared to conventional GI and CCD/CMOS

imaging, LMS-GI’s imaging quality is significantly improved. As a result, LMS-GI can be used as an imaging solution in challenging liquid environments, including turbid liquids, inclement weather, and biological tissue fluids.

Table 1 | Comparison of laser mode speckle pattern ghost imaging (LMS-GI) with other ghost imaging techniques for turbid underwater imaging

Year	Algorithm	Water quality (turbidity)	Sampling rate
2017 ³⁸	correlation calculation	china clay (80 NTU)	-
2019 ³⁹	correlation calculation	black ink (0.4 mL)	-
2020 ⁴⁰	correlation calculation	milk (milk: water = 1:1500, 32 FTU)	1
2021 ⁴¹	correlation calculation	kaolin clay powder (80 NTU)	20%
2021 ¹⁰	deep learning	milk (milk: water < 1:6.84)	20%
2021 ¹¹	compressed sensing	milk (milk: water = 1:9)	2%–5%
Our LMS-GI method	correlation calculation	milk (milk: water < 1:7)	0.64%–2.48%

Methods

Ghost imaging

The object has a resolution of $n_1 \times n_2$, and the transmission distribution of the object is $T(x, y)$, where $x = 1, 2, \dots, n_1, y = 1, 2, \dots, n_2$ which can be converted to a matrix of $n \times 1$ dimension X , where $n = n_1 n_2$. The resolution of each scattergram is $n_1 \times n_2$, the amount of projected speckle data is m , and the light intensity distribution of the t -th speckle pattern is $I(x, y, t)$, where $t = 1, 2, \dots, m$, converting the array of speckle patterns into Φ , which is a matrix of $m \times n$ dimension. And the corresponding t -h bucket detector value is:

$$B(t) = \iint I(x, y, t)T(x, y)dxdy \tag{13}$$

Form the light intensity collected by a bucket detector into a $m \times 1$ matrix Y . The imaging process of GI is:

$$Y = \Phi X \tag{14}$$

The mean value of the m bucket detectors is:

$$\langle B \rangle = \frac{1}{m} \sum_{t=1}^m B(t) \tag{15}$$

The mean value of the speckle patterns is:

$$\langle I \rangle = \frac{1}{m} \sum_{t=1}^m I(x, y, t) \tag{16}$$

Using the second-order correlation for the calculation, the GI is obtained as:

$$G(x, y) = \frac{1}{m} \sum_{t=1}^m \{ [B(t) - \langle B \rangle][I(x, y, t) - \langle I \rangle] \} \tag{17}$$

Statistics and reproducibility

In Fig. 7, the bucket detector updates its value every 1 s, with 0.5 s allocated for averaging to ensure data reliability.

Laser mode evaluation criteria M^2

The M^2 factor has become one of the most widely accepted parameters for evaluating beam quality. The beam radii of the H – G_{mn} modes in the x and

y directions are:

$$\begin{aligned} w_{x,mn}^2(z) &= \frac{4 \int_{-\infty}^{+\infty} x^2 H_m^2 \left(\frac{\sqrt{2}x}{w_{os}} \right) e^{-\frac{2x^2}{w_{os}^2}} dx}{\int_{-\infty}^{+\infty} H_m^2 \left(\frac{\sqrt{2}x}{w_{os}} \right) e^{-\frac{2x^2}{w_{os}^2}} dx} \\ &= (2m + 1)w_{os}^2(z) \\ w_{y,mn}^2(z) &= \frac{4 \int_{-\infty}^{+\infty} y^2 H_n^2 \left(\frac{\sqrt{2}y}{w_{os}} \right) e^{-\frac{2y^2}{w_{os}^2}} dy}{\int_{-\infty}^{+\infty} H_n^2 \left(\frac{\sqrt{2}y}{w_{os}} \right) e^{-\frac{2y^2}{w_{os}^2}} dy} \\ &= (2n + 1)w_{os}^2(z) \end{aligned} \tag{18}$$

The beam radius of the H – G_{mn} mode in r radial direction is:

$$\begin{aligned} w_{r,mn}^2(z) &= \frac{4 \int_{-\infty}^{+\infty} \int_{-\infty}^{+\infty} (x^2 + y^2) H_m^2 \left(\frac{\sqrt{2}x}{w_{os}} \right) H_n^2 \left(\frac{\sqrt{2}y}{w_{os}} \right) e^{-\frac{2(x^2+y^2)}{w_{os}^2}} dx dy}{\int_{-\infty}^{+\infty} \int_{-\infty}^{+\infty} H_m^2 \left(\frac{\sqrt{2}x}{w_{os}} \right) H_n^2 \left(\frac{\sqrt{2}y}{w_{os}} \right) e^{-\frac{2(x^2+y^2)}{w_{os}^2}} dx dy} \\ &= 2(m + n + 1)w_{os}^2(z) \end{aligned} \tag{19}$$

The waist half-width and far-field divergence half-angle of the fundamental mode Gaussian beam are set as w_0 and θ_0 , and

$$w_0 \theta_0 = \frac{\lambda}{\pi} \tag{20}$$

The half-widths of H – G_{mn} bundle waist in the x direction, y direction, and r radial direction are:

$$\begin{cases} w_{0x,mn}^2 = (2m + 1)w_0^2 \\ w_{0y,mn}^2 = (2n + 1)w_0^2 \\ w_{0r,mn}^2 = 2(m + n + 1)w_0^2 \end{cases} \tag{21}$$

The far-field diverging half-angles of H – G_{mn} in the x direction, y direction, and r radial direction are:

$$\begin{cases} \theta_{x,mn} = \lim_{z \rightarrow \infty} \frac{w_{x,mn}(z)}{z} = \sqrt{2m + 1} \lim_{z \rightarrow \infty} \frac{w(z)}{z} \\ = \sqrt{2m + 1} \frac{\lambda}{\pi w_0} = \sqrt{2m + 1} \theta_0 \\ \theta_{y,mn} = \lim_{z \rightarrow \infty} \frac{w_{y,mn}(z)}{z} = \sqrt{2n + 1} \lim_{z \rightarrow \infty} \frac{w(z)}{z} \\ = \sqrt{2n + 1} \frac{\lambda}{\pi w_0} = \sqrt{2n + 1} \theta_0 \\ \theta_{r,mn} = \lim_{z \rightarrow \infty} \frac{w_{r,mn}(z)}{z} = \sqrt{(2m + 1)(2n + 1)} \lim_{z \rightarrow \infty} \frac{w(z)}{z} \\ = \sqrt{(2m + 1)(2n + 1)} \frac{\lambda}{\pi w_0} = \sqrt{(2m + 1)(2n + 1)} \theta_0 \end{cases} \tag{22}$$

The M^2 factors in the x direction, y direction, and r radial direction of $H - G_{mn}$ can be expressed as:

$$\begin{cases} M_x^2 = \frac{\pi}{\lambda} w_{0x} \theta_x = \frac{\pi}{\lambda} \sqrt{2m+1} w_0 \sqrt{2m+1} \theta_0 = 2m+1 \\ M_y^2 = \frac{\pi}{\lambda} w_{0y} \theta_y = \frac{\pi}{\lambda} \sqrt{2n+1} w_0 \sqrt{2n+1} \theta_0 = 2n+1 \\ M_r^2 = \frac{\pi}{\lambda} w_{0r} \theta_r = \frac{\pi}{\lambda} \sqrt{(2n+1)(2m+1)} w_0 \sqrt{(2n+1)(2m+1)} \theta_0 \\ = 2(m+n+1) \end{cases} \quad (23)$$

Data availability

The data that support the findings of this study are available from the corresponding author upon request.

Code availability

All codes used in this study are available from the corresponding authors upon request.

Received: 19 April 2023; Accepted: 12 March 2024;

Published online: 21 March 2024

References

- Klein, Y., Sefi, O., Schwartz, H. & Shwartz, S. Chemical element mapping by X-ray computational ghost fluorescence. *Optica* **9**, 63–70, (2022).
- Tan, Z. et al. Single-exposure Fourier-transform ghost imaging based on spatial correlation. *Phys. Rev. A* **106**, 053521 (2022).
- Olivieri, L. et al. Hyperspectral terahertz microscopy via nonlinear ghost imaging. *Optica* **7**, 186–191, (2020).
- Tian, Y. et al. Acoustic ghost imaging in the time domain. *Phys. Rev. Appl.* **13**, 064044 (2020).
- Sun, B. et al. 3D computational imaging with single-pixel detectors. *Science* **340**, 844–847 (2013).
- Hong, P. & Liang, Y. Three-dimensional microscopic single-pixel imaging with chaotic light. *Phys. Rev. A* **105**, 023506 (2022).
- Zhang, L., Wang, Y. & Zhang, D. Research on multiple-image encryption mechanism based on Radon transform and ghost imaging. *Opt. Commun.* **504**, 127494 (2022).
- Sui, L. et al. An optical image encryption based on computational ghost imaging with sparse reconstruction. *Opt. Lasers Eng.* **143**, 106627 (2021).
- Wang, M. et al. Effect of uneven temperature distribution on underwater computational ghost imaging. *Laser Phys.* **32**, 065205 (2022).
- Yang, X. et al. Underwater ghost imaging based on generative adversarial networks with high imaging quality. *Opt. Express* **29**, 28388–28405 (2021).
- Wang, T. et al. Underwater compressive computational ghost imaging with wavelet enhancement. *Appl. Opt.* **60**, 6950–6957 (2021).
- Wu, H., Zhao, G., He, C., Cheng, L. & Luo, S. Sub-Nyquist underwater denoising ghost imaging with a Coiflet-wavelet-order-based Hadamard matrix. *Phys. Rev. A* **106**, 053522 (2022).
- Yin, M.-Q., Wang, L. & Zhao, S.-M. Experimental demonstration of influence of underwater turbulence on ghost imaging. *Chin. Phys. B* **28**, 094201 (2019).
- Wu, H., Chen, Z., He, C., Cheng, L. & Luo, S. Experimental study of ghost imaging in underwater environment. *Sensors* **22**, 8951 (2022).
- Afzal, S. S. et al. Battery-free wireless imaging of underwater environments. *Nat. Commun.* **13**, 1–9 (2022).
- Shapiro, J. H. Computational ghost imaging. *Phys. Rev. A* **78**, 061802(R) (2008).
- Kingston, A. M. et al. Optimizing nonconfigurable, transversely displaced masks for illumination patterns in classical ghost imaging. *Phys. Rev. A* **107**, 023524 (2023).
- Ceddia, D. & Paganin, D. M. Random-matrix bases, ghost imaging, and x-ray phase contrast computational ghost imaging. *Phys. Rev. A* **97**, 062119 (2018).
- Wang, C., Gong, W., Shao, X. & Han, S. The influence of the property of random coded patterns on fluctuation-correlation ghost imaging. *J. Opt.* **18**, 065703 (2016).
- Nie, X. et al. Noise-robust computational ghost imaging with pink noise speckle patterns. *Phys. Rev. A* **104**, 013513 (2021).
- Zhang, Z., Wang, X., Zheng, G. & Zhong, J. Hadamard single-pixel imaging versus Fourier single-pixel imaging. *Opt. Express* **25**, 19619–19639 (2017).
- Yuan, X., Zhang, L., Chen, J., Wang, K. & Zhang, D. Multiple-image encryption scheme based on ghost imaging of Hadamard matrix and spatial multiplexing. *Appl. Phys. B* **125**, 1–13 (2019).
- Wang, L. & Zhao, S. Fast reconstructed and high-quality ghost imaging with fast Walsh–Hadamard transform. *Photon. Res.* **4**, 240–244 (2016).
- Wu, H. et al. Influence of intensity fluctuations on Hadamard-based computational ghost imaging. *Opt. Commun.* **454**, 124490 (2020).
- Yu, Z., Gao, C., Wang, X.-Q., Zhao, H. & Yao, Z.-H. Hadamard-Haar (2D) dual domain ghost imaging. *Opt. Laser Technol.* **155**, 108413 (2022).
- Choudhury, D. et al. Computational optical imaging with a photonic lantern. *Nat. Commun.* **11**, 1–9 (2020).
- Sun, Y. et al. Cosinusoidal encoding multiplexed structured illumination multispectral ghost imaging. *Opt. Express* **30**, 31728–31741 (2022).
- Nie, X., Zhao, X., Peng, T. & Scully, M. O. Sub-Nyquist computational ghost imaging with orthonormal spectrum-encoded speckle patterns. *Phys. Rev. A* **105**, 043525 (2022).
- Siegman, A. E. & Townsend, S. W. Output beam propagation and beam quality from a multimode stable-cavity laser. *IEEE J. Quant. Electron.* **29**, 1212–1217 (1993).
- Siegman, A. E. Defining, measuring, and optimizing laser beam quality. *Proceedings: Laser Resonators and Coherent Optics: Modeling, Technology, and Applications*. Vol. 1868. 2–12 (SPIE, 1993).
- Siegman, A. E. New developments in optical resonators. Vol. 1224. 2–14 (SPIE, 1990).
- Fang, T., Ye, X., Niu, J. & Xu, J. Definition and measurement of the beam propagation factor M^2 for chromatic laser beams. *Chin. Opt. Lett.* **4**, 586–588 (2006).
- Paschotta, R. Beam quality deterioration of lasers caused by intracavity beam distortions. *Opt. Express* **14**, 6069–6074 (2006).
- Borgentun, C., Bengtsson, J. & Larsson, A. Full characterization of a high-power semiconductor disk laser beam with simultaneous capture of optimally sized focus and farfield. *Appl. Opt.* **50**, 1640–1649 (2011).
- Feng, G., Zhou, S. & Gao, C. *Laser Mode Field and Beam Quality Characterization* (National Defense Industry Press, 2016).
- Liu, H.-C. et al. Single-pixel computational ghost imaging with helicity-dependent metasurface hologram. *Sci. Adv.* **3**, e1701477 (2017).
- Sara, U., Akter, M. & Uddin, M. S. Image quality assessment through FSIM, SSIM, MSE and PSNR—a comparative study. *J. Comput. Commun.* **7**, 8–18 (2019).
- Le, M. et al. Underwater computational ghost imaging. *Opt. Express* **25**, 22859–22868, (2017).
- Zhang, Y. et al. High-visibility underwater ghost imaging in low illumination. *Opt. Commun.* **441**, 45–48 (2019).
- Wu, H., Zhao, M., Li, F., Tian, Z. & Zhao, M. Underwater polarization-based single pixel imaging. *J. Soc. Inf. Disp.* **28**, 157–163 (2020).
- Yang, X. et al. Imaging in turbid water based on a Hadamard single-pixel imaging system. *Opt. Express* **29**, 12010–12023, (2021).

Acknowledgements

The authors acknowledge support from the National Key Research and Development Program of China (No. 2022YFB3606304) and the National Natural Science Foundation of China (No. U2230129).

Author contributions

Mo-Chou Yang (idea construction, simulation calculations, experiment completion, chart drawing, first draft completion, and manuscript modification). Guo-Ying Feng (main construction of idea, drawing of diagram, revision of the manuscript). Yi Wu (completion of the experiment) and Peng Wang (model calculation).

Competing interests

The authors declare no competing interests.

Additional information

Correspondence and requests for materials should be addressed to Guo-Ying Feng.

Peer review information *Communications Engineering* thanks Heng Wu and the other, anonymous, reviewer(s) for their contribution to the peer review of this work. Primary handling editors: Mengying Su, Rosamund Daw.

Reprints and permissions information is available at <http://www.nature.com/reprints>

Publisher's note Springer Nature remains neutral with regard to jurisdictional claims in published maps and institutional affiliations.

Open Access This article is licensed under a Creative Commons Attribution 4.0 International License, which permits use, sharing, adaptation, distribution and reproduction in any medium or format, as long as you give appropriate credit to the original author(s) and the source, provide a link to the Creative Commons licence, and indicate if changes were made. The images or other third party material in this article are included in the article's Creative Commons licence, unless indicated otherwise in a credit line to the material. If material is not included in the article's Creative Commons licence and your intended use is not permitted by statutory regulation or exceeds the permitted use, you will need to obtain permission directly from the copyright holder. To view a copy of this licence, visit <http://creativecommons.org/licenses/by/4.0/>.

© The Author(s) 2024